

X-Ray Phase-Contrast Imaging

3	Grating-Based X-Ray Phase-Contrast Imaging <i>Peter Modregger, Bernd Pinzer, Zhentian Wang, and Marco Stampanoni</i>	43
	Introduction • Elements of the Image Formation Process • Experimental Implementation • Biomedical Research and Potential Clinical Application • Acknowledgments • References	
4	Analyzer-Based X-Ray Phase-Contrast Imaging <i>Jovan G. Brankov and Adam M. Zysk</i>	57
	Introduction • Imaging Principles • Biological and Medical Applications • Image Formation Model • Methods for Estimation of Parametric Images • Computed Tomography Methods • Benchtop Systems • Future Challenges • Appendix A: Bragg's Law • Appendix B: Image Formation Model • References	
5	Propagation-Based Imaging <i>Glenn R. Myers, Karen K.W. Siu, and Kaye S. Morgan</i>	75
	Overview and Clinical Potential • Qualitative Imaging: Phase Contrast • Quantitative Imaging: Phase Retrieval • Biomedical Applications of Propagation-Based Imaging • Summary • References	

Grating-Based X-Ray Phase-Contrast Imaging

Peter Modregger
Paul Scherrer Institute
University of Lausanne

Bernd Pinzer
Paul Scherrer Institute

Zhentian Wang
Paul Scherrer Institute

Marco Stampanoni
Paul Scherrer Institute
ETH and University of Zürich

3.1	Introduction	43
3.2	Elements of the Image Formation Process	44
	Fresnel Diffraction at Periodic Structures • Data Analysis Procedures and Complementary Contrasts	
3.3	Experimental Implementation	49
	Influence of Finite Coherence • Instruments Utilizing Synchrotron Radiation • Instruments Based on X-Ray Tubes • Grating Manufacturing	
3.4	Biomedical Research and Potential Clinical Application	52
	Imaging Aortic Heart Valve Calcifications • Imaging Alzheimer's Plaque Deposits in a Mouse Model • Potential for Mammography	
	Acknowledgments	55
	References	55

3.1 Introduction

Since its first experimental demonstration in 2002/2003 (David et al., 2002; Momose et al., 2003), the phase-sensitive, hard x-ray imaging technique called *grating interferometry* (GI) has attracted increasing interest from researchers in a wide variety of fields. This interest is due to the unique combination of advantageous imaging characteristics offered by GI. The following three characteristics may be identified as the major contributing factors. First, GI provides a particularly high sensitivity to electron-density variations, which allows for imaging subtle differences within a sample. It has been experimentally demonstrated that electron-density variations down to 0.18 e nm^{-3} are observable (Pfeiffer et al., 2007a). This renders GI especially suitable for soft-tissue specimens from the field of biomedical research. Destruction-free x-ray imaging with GI has been successfully applied to biological samples and tissues such as insects (Pfeiffer et al., 2007c; Weitkamp et al., 2005), rat brains (McDonald et al., 2009; Müller et al., 2008), rat liver (Momose et al., 2006), myocardial structures (Bech et al., 2009), and even human tissues such as breast tissue (Chen et al., 2010b; Stampanoni et al., 2011) and the cerebellum (Schulz et al., 2010).

Second, GI simultaneously provides three complementary types of information about the sample. The absorption contrast relates to the “classic” x-ray image, which is based on variations of the linear attenuation coefficient. The (differential) phase contrast (DPC) is proportional to the (first derivative of the) accumulated phase shift of the x-ray beam after transmission through the sample. The DPC signal is mainly responsible for the high sensitivity of GI (McDonald et al., 2009). The so-called scatter contrast

(also dark-field or visibility-reduction contrast) is a measure of the scatter strength of specific sample details (Pfeiffer et al., 2008), and its origin as well as its interpretation is the subject of ongoing research (Lynch et al., 2011; Yashiro et al., 2010). These complementary contrasts can be taken advantage of in order to increase the ability to detect and discriminate between minute sample variations (Bech et al., 2010; Stampanoni et al., 2011).

Third and most important for the potential broad application of the technique, GI features a comparably low requirement for the spectral width of the utilized x-ray beam, which allows GI to be nearly achromatic (Engelhardt et al., 2008; Weitkamp et al., 2005). This particular advantage yields the possibility of using an x-ray tube as the source (Engelhardt et al., 2007; Pfeiffer et al., 2006), which is accompanied by the amenities of low cost and ready accessibility.

It is the combination of high sensitivity, the availability of complementary contrasts, and the possibility of implementing the GI in a laboratory setup that strongly suggests its future widespread application in materials sciences (e.g., material testing), biomedical research (e.g., monitoring drug effects), or even clinical diagnostics (e.g., mammography).

The basic principle of any phase-sensitive imaging technique lies with the description of the contrast formation process in terms of the complex wave. A complex wave is characterized by the combination of intensity and phase, but in experimental practice, only the intensity is directly accessible. Thus, the experimental setup must offer the capability to transform phase contrast into a detectable intensity contrast in order to provide phase sensitivity. For GI, this is realized in the following way.

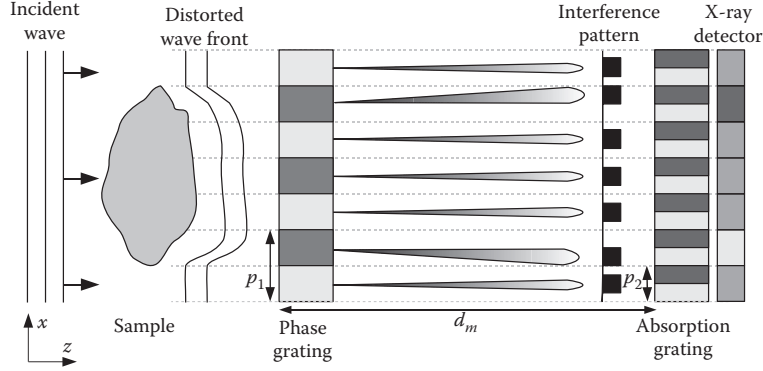


FIGURE 3.1 Sketch of an x-ray grating interferometer.

The GI consists of two line gratings, which are positioned downstream of the sample (see Figure 3.1). The first line grating acts as a beam splitter, dividing the incident beam into several diffraction orders. Due to the coherence of the beam, these diffraction orders interfere constructively at certain distances d downstream of the beam splitter. This provides a rectangular-shaped interference pattern. Placing a sample in front of the first line grating introduces refraction into the beam, which leads to a lateral offset of the interference pattern. Since the period of the interference pattern is too small to be resolved by standard x-ray detectors, a second line grating of purely absorbing structures is used to analyze the interference pattern. The pitch of the absorption grating matches the period of the interference pattern and a lateral offset of the interference pattern is translated into a change of intensity at the detector. Since the lateral offset is proportional to the refraction angle and the refraction angle is, in turn, proportional to the first derivative of the phase of the wave after transmission through the sample, DPC is observed at the detector.

The goal of this presentation is to introduce the reader to the basic concepts of x-ray imaging with GI, thus providing sufficient understanding in order to appreciate the exciting potential benefits of this imaging technique. In Section 3.2, we present the fundamentals of x-ray imaging with GI. We will focus on the theoretical description of the image formation process, on postdetection analysis algorithms and the interpretation of the complementary contrasts. In Section 3.3, the most common variants of experimental implementation of GI will be introduced. Finally, Section 3.4 will present prominent examples of the successful application of GI in the field of biomedical research and the potential of GI for mammography will be discussed.

3.2 Elements of the Image Formation Process

As described in the introduction, the principle of GI is based on the occurrence of a rectangular-shaped interference pattern whose formation process is presented in more detail in the following. Additionally, this section describes the scan and data

analysis procedures that are utilized in order to retrieve the three complementary contrasts.

3.2.1 Fresnel Diffraction at Periodic Structures

First discovered by Talbot (1836) and later explained by Rayleigh (1881), the so-called *Talbot effect* relates to coherent diffraction at periodic structures. At certain distances downstream of the diffracting object, self-images of the periodic structure can be observed. In the case of GI, the beam splitter provides a periodic interference pattern and it can be realized by either an absorption grating, which is described by the integer Talbot effect, or more commonly by a phase grating, which is described by the fractional Talbot effect.

For reasons of simplicity, the discussion will be limited to the one-dimensional case and since only relative intensities are of interest, global phase terms as well as constant factors will be omitted. Further, in this section, a monochromatic and collimated incident beam (i.e., the case of perfect coherence) is assumed.

3.2.1.1 Integer Talbot Effect

The interaction of x-rays with matter is described by the complex refractive index $n = 1 - \delta + i\beta$, with δ the refractive index decrement, which corresponds to phase contrast, and β the extinction coefficient, which quantifies the absorption contrast. The complex wave amplitude directly after transmission through the sample, denoted by $D_{\text{in}}(x)$, is given by the integration of the refraction index over the beam path (see Figure 3.1):

$$D_{\text{in}}(x) = \exp\left(\int i k n(x, z) dz\right) \quad (3.1)$$

with $k = 2\pi/\lambda$ being the wavenumber and λ the wavelength. The Fresnel diffraction integral (Born and Wolf, 1999) relates $D_{\text{in}}(x)$ to the complex wave amplitude $D_{\text{out}}(x)$, which is observable after free-space propagation over the distance z :

$$D_{\text{out}}(x) = \int dq \hat{D}_{\text{in}}(q) \exp\left(-i \frac{q^2}{2k} z\right) \exp(iqx). \quad (3.2)$$

$\hat{D}_{\text{in}}(q)$ denotes the Fourier transform of $D_{\text{in}}(x)$. If $D_{\text{in}}(x)$ describes a periodic diffracting structure with period p_1 (e.g., the first line grating), then its Fourier transform is discrete:

$$\hat{D}_{\text{in}}(q) = \sum_m \hat{G}(q) \delta(q - q_m) \quad (3.3)$$

with $\hat{G}(q)$ the Fourier transform of the structure within one period. $\hat{D}_{\text{in}}(q)$ is only nonzero for the spatial frequencies:

$$q_m = m \frac{2\pi}{p_1} \quad \text{with } m \in \mathbb{Z}. \quad (3.4)$$

Inserting Equation 3.3 in Equation 3.2 demonstrates that the propagated wave amplitude $D_{\text{out}}(x)$ differs from the input wave field $\hat{D}_{\text{in}}(q)$ only by the factor $\exp(-izq_m^2/2k)$. For multiples $z_n = n\tau$ ($n \in \mathbb{Z}$) of the Talbot distance τ

$$\tau = \frac{p_1^2}{2\lambda}, \quad (3.5)$$

this factor equals one and, thus, the original wave field D_{in} is again observable. If the diffracting structure comprises a line grating with purely absorbing structures, the corresponding self-image forms the desired rectangular-shaped interference pattern. Figure 3.2a shows the interference pattern of an absorption grating at different propagation distances (given in terms

of n), which is—for obvious reasons—called *the Talbot carpet*. The visibility of the interference pattern is optimal for all integer multiples of the Talbot distance and, thus, these positions would be used in experimental practice.

3.2.1.2 Fractional Talbot Effect

In terms of detection efficiency, the utilization of a beam splitter with absorbing line structures is undesirable. Half of the photons that are transmitted through the sample would be absorbed in the beam-splitter grating and could not contribute to the signal at the detector. But fortunately, the beam splitter can also be realized by a phase-shifting grating, which avoids the unfavorable absorption.

This possibility is based on the *fractional Talbot effect*, which describes Fresnel diffraction at propagation distances that are given as fractions of the Talbot distance τ , that is

$$z = \frac{n_1}{n_2} \tau \quad \text{with } n_1, n_2 \in \mathbb{N}. \quad (3.6)$$

Inserting Equations 3.3 through 3.6 into Equation 3.2 and using Gauss' sum of number theory (i.e., $\exp(-i2\pi \frac{n_1}{n_2} m^2) = \sum_{s=0}^{l-1} c_s \exp(-i2\pi m \frac{s}{l})$) (Banaszek et al., 1997)) leads to

$$D_{\text{out}}(x) = \sum_m \hat{G}(q_m) e^{iq_m x} \sum_{s=0}^{l-1} c_s e^{-i2\pi m \frac{s}{l}} \quad (3.7)$$

with $l \leq n_2$. Equation 3.7 can be understood as a superposition of l copies of the original amplitude, each weighted with the factor

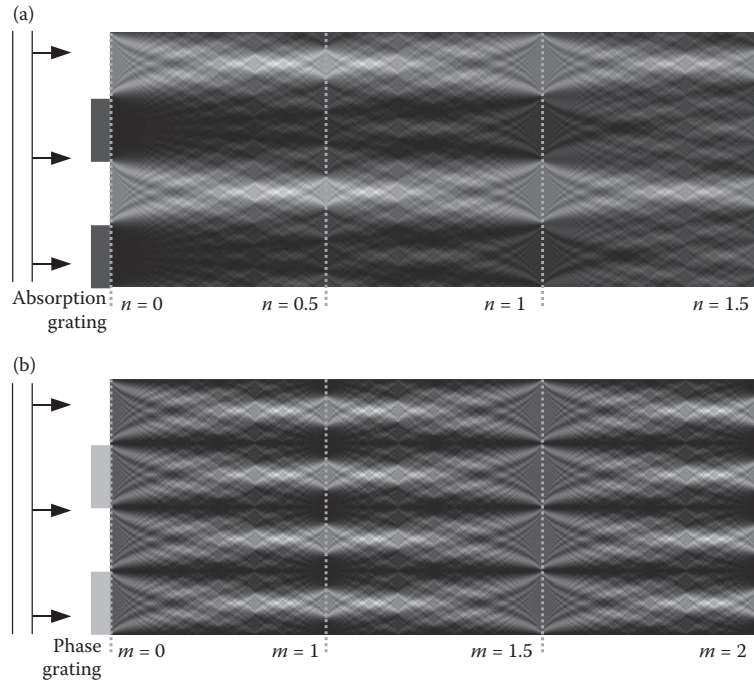


FIGURE 3.2 Talbot carpets for (a) an absorption grating and (b) a phase grating.

$cs = c_s(n_1, n_2)$ and separated by the fraction s/l of the period. As an example, let us consider $l = 4$, which corresponds to $z = \tau/4$, and a beam-splitter grating that shifts the phase of the incident wave by π . In this case, $c_0 = 1$, $c_1 = 0$, $c_2 = 1$, and $c_3 = 0$ holds true and the observable wave amplitude is given by two copies of the original amplitude shifted by half a period. Due to the interference of the two copies, the result will be an observable rectangular-shaped interference pattern with half of the period. An overview of experimental conditions for phase gratings utilizing different phase shifts can be found in Suleski (1997).

In case of a π -shifting phase grating, the rectangular-shaped interference pattern is located at the so-called Lohmann distances d_m

$$d_m = \left(m - \frac{1}{2}\right) \frac{p_1^2}{4\lambda} \quad \text{with } m = 1, 2, \dots \quad (3.8)$$

with m the Lohmann diffraction order. The corresponding Talbot carpet is shown in Figure 3.2b. Please note the varying definitions of the diffraction order in literature (see, e.g., Weitkamp et al., (2005)).

3.2.2 Data Analysis Procedures and Complementary Contrasts

GI realizes phase sensitivity in the following way. The sample introduces refraction into the incident wave and, consequently, shifts the interference pattern laterally. This lateral shift Δx is proportional to the refraction angle α (i.e., $\Delta x \approx d\alpha$). In turn, the refraction angle is proportional to the first derivative of the

phase of the complex wave amplitude after transmission through the sample Φ (see Born and Wolf (1999)):

$$\alpha = -\frac{1}{k} \frac{\partial \Phi}{\partial x}. \quad (3.9)$$

Therefore, (differential) phase sensitivity is established if the lateral shift of the interference pattern can be detected. However, in order to provide high sensitivity, the period of the rectangular-shaped interference pattern is typically around a few microns, which is too small to be resolved by standard x-ray detectors. For this reason, an analyzer grating of purely absorbing line structures is utilized (see Figure 3.1), which essentially scales up the information that is encoded in the interference pattern. In order to maximize the visibility, the pitch p_2 of the analyzer grating should match the period of the interference pattern, that is, $p_2 = p_1/2$ for a π -shifting phase grating and a parallel-beam geometry. Refraction and, thus, phase information becomes visible as brightening and darkening of the corresponding detector pixels (Figure 3.1).

The so-called *phase-stepping technique* constitutes the most widely used scan and data analysis scheme for GI. The scan is performed by laterally scanning one of the gratings in steps that are a fraction of the grating's pitch and acquiring an image at each step. In doing so, at each pixel, one measures a phase-stepping curve (PSC) that shows an oscillatory behavior (Figure 3.3a). This can be understood by realizing that the lateral scan of a rectangular function (e.g., the interference pattern) over another rectangular function (e.g., the transmission function of the analyzer grating) is equivalent to the convolution of the two functions. Thus, the result is an oscillatory triangular function. However, due to the effects of finite spatial coherence, the

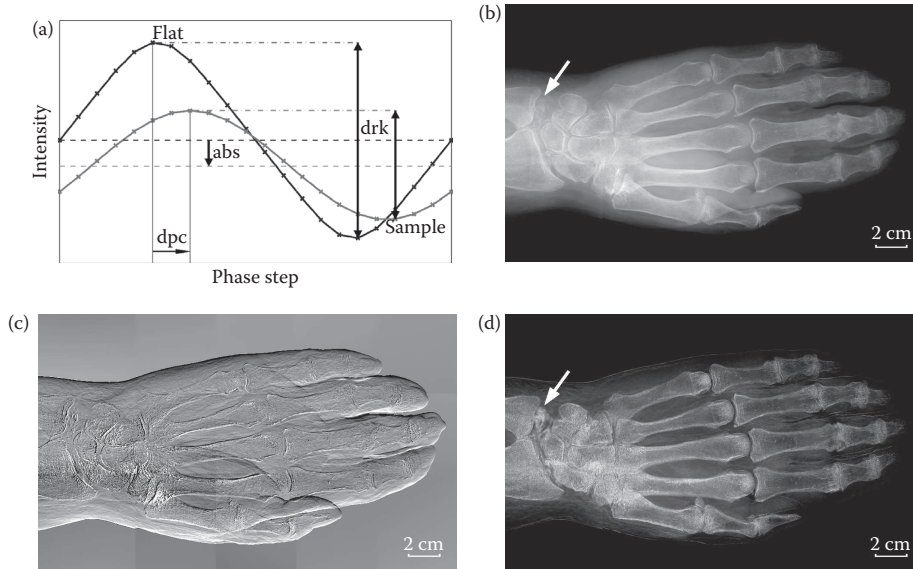


FIGURE 3.3 (a) Phase-stepping curves and extraction of contrasts. Radiographs for three different contrasts of a human hand: (b) absorption, (c) differential phase, and (d) scatter contrast.

interference pattern will not be perfectly rectangular, and thus the convolved pattern will be more sinusoidal than triangular, as depicted in Figure 3.3a.

The resulting PSC can be approximated by a first-order Fourier expansion (Momose, 2004):

$$\text{PSC}(\phi) \approx a + b \sin(\phi - p), \quad (3.10)$$

where ϕ is the lateral offset of the phase step in terms of radians. The other parameters correspond to the complementary contrasts (Figure 3.3) that are provided by GI. a is the mean of the PSC and relates to the absorption contrast. b is connected to the scatter contrast and denotes the amplitude of the PSC. p constitutes the offset or phase of the PSC and relates to the (differential) phase contrast.

Usually, a flat-field PSC, $f(\phi)$, without the sample, and a sample PSC, $s(\phi)$, are acquired. The parameters a , b , and p are determined by a Fourier analysis approach, which is mathematically equivalent to a least-squares fit. The so-called Fourier-component analysis starts with a discrete Fourier transform of the PSCs with respect to the phase steps ϕ yielding $\hat{f}(q)$ and $\hat{s}(q)$. In the following, the subsequent steps to retrieve the individual contrasts will be discussed separately.

3.2.2.1 Absorption Contrast

The absorption contrast is calculated by

$$A = \frac{\hat{s}(q_0)}{\hat{f}(q_0)} \quad (3.11)$$

with q_0 the zeroth harmonic Fourier component. By taking the negative logarithm of each projection, A is related to the attenuation coefficient β via the line integral

$$-\log A(x) = k \int \beta(x, z) dz, \quad (3.12)$$

where the beam direction is along z . Thus, the Fourier slice theorem is applicable (Kak and Slaney, 1988), and the 2D distribution of the attenuation coefficient β can be tomographically reconstructed. In Qi et al. (2010), it was presented that β may be expressed as

$$\beta = (\bar{m}Z^{\bar{n}} + \bar{b})\rho_e \quad (3.13)$$

with ρ_e , the electron density, Z , the effective atomic number, and $\bar{m}, \bar{n}, \bar{b}$ parameters that depend only on the details of experimental implementation and not on sample properties.

3.2.2.2 Differential Phase Contrast

The DPC is determined by

$$P = \arg(\hat{s}(q_n)) - \arg(\hat{f}(q_n)) \quad (3.14)$$

with q_n the n -th harmonic Fourier component and n equal to the number of scanned PSC periods. The obtained DPC value is related to the refraction angle by

$$P = 2\pi \frac{d_m \alpha}{p_2}. \quad (3.15)$$

However, if the lateral offset Δx of the interference pattern becomes larger than the pitch of the analyzer grating, phase wrapping occurs (Modregger et al., 2011a). This means that P -values outside of the interval $[-\pi, \pi]$ are falsely translated into this interval. An example of phase wrapping is visible in Figure 3.3c as the strong dark/bright contrast at the edges of the hand. Naturally, phase wrapping leads to severe artifacts and, thus, should be avoided if possible. Recently, an approximate correction algorithm has been proposed that utilizes the absorption contrast as a predictor for the phase contrast (Jerjen et al., 2011).

Equation 3.15 also reveals the importance of realizing an interference pattern with the smallest possible period p_2 . Since the maximum of P is π and d_m is typically several decimeters, the interference pattern must have a pitch of few micrometers in order to observe nano-radian refraction angles. By fulfilling this experimental condition, it was demonstrated that minute refraction angles of only 17 nrad are detectable by GI (Pfeiffer et al., 2007a).

The DPC value P is related to the first derivative of the line integral over the refractive index decrement δ , that is

$$P(x) = \frac{\partial}{\partial x} k \int \delta(x, z) dz. \quad (3.16)$$

It has been shown that a modified version of the Fourier slice theorem can account for the differential nature of the phase contrast (Pfeiffer et al., 2007b). Thus, the 2D distribution of the refractive index decrement δ can be reconstructed. For a given photon energy E , δ is given by

$$\delta = \frac{r_0 \hbar^2 c^2}{2\pi E^2} \rho_e \quad (3.17)$$

with r_0 the classical electron radius, \hbar the reduced Planck's constant, and c the speed of light. Comparing Equation 3.13 with Equation 3.17 reveals the complementary nature of the absorption and the phase contrast. While the absorption contrast is proportional to the product $\rho_e Z^n$, the phase contrast depends only on the electron density ρ_e .

3.2.2.3 Scatter Contrast

Finally, the scatter contrast (also called dark-field (Pfeiffer et al., 2008) or visibility reduction contrast (Yashiro et al., 2010)) is retrieved by

$$B = \frac{\hat{s}(q_n) \hat{f}(q_0)}{\hat{s}(q_0) \hat{f}(q_n)}. \quad (3.18)$$

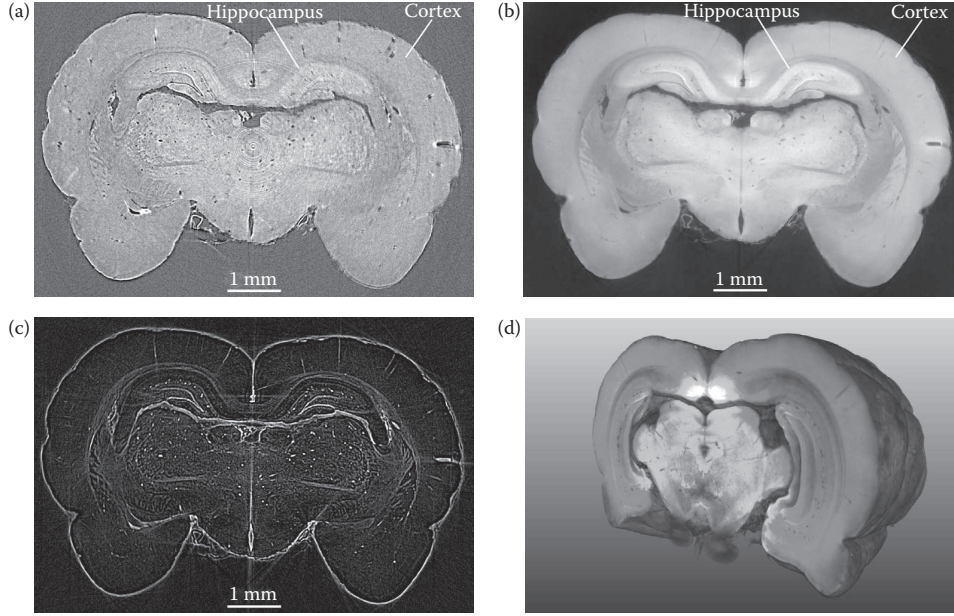


FIGURE 3.4 Tomographic reconstructions of the complementary contrasts provided by grating interferometry of a paraffin-embedded rat brain: (a) absorption contrast, (b) phase contrast, (c) scatter contrast, and (d) a 3D visualization of the phase-contrast data.

Based on the assumption that the scattering of the x-rays is isotropic and describable by a Gaussian distribution, it was demonstrated (Khelashvili et al., 2006) that the scattering width σ fulfills the line integral

$$\sigma(x)^2 = \int S(x, z) dz \quad (3.19)$$

with S a generalized scattering parameter that quantifies the local scatter strength. Since the scattering width σ is related to the scatter contrast by (Wang et al., 2009)

$$\sigma^2 = -\frac{1}{2\pi^2} \left(\frac{p_2}{d_m} \right)^2 \ln B, \quad (3.20)$$

the 2D distribution of S may be tomographically reconstructed in a way that closely resembles the procedure for the absorption contrast. However, if the assumption of isotropic Gaussian scattering is violated, artifacts appear in the reconstructions (Modregger et al., 2011b).

The physical interpretation of the scatter contrast is still being investigated. So far, it is clear that the scatter contrast corresponds to the width of the underlying but unresolved scatter distribution within a detector pixel (Modregger et al., 2012a; Yashiro et al., 2010). Recent investigations also suggest that the scatter contrast provides particle size sensitivity (Lynch et al., 2011).

Figure 3.3 shows the radiographs for the complementary contrasts of a human hand, which were retrieved by GI. Soft tissue is enhanced in the DPC image (Figure 3.3c), while the hand

bones are clearly visible in the absorption as well as in the scatter image. While the soft tissue provides a still well-defined signal in the absorption contrast, the scattering of the tissue is obviously too weak to produce a significant contribution to the scatter contrast. So, generally, although bones are already well represented in absorption contrast, scatter imaging can potentially yield a complementary and even enhanced contrast, as shown by the soft-tissue calcification in the region of the triangular fibrocartilage (indicated by the arrows).

Figure 3.4 shows tomographic reconstructions of the complementary contrasts for a paraffin-embedded rat brain. The sample consists mainly of low- Z material and in such a case the superiority of the phase contrast over the absorption contrast is apparent by the visible noise in the images. Further, the contrast between morphological regions of the brain (e.g., cortex and hippocampus) is much better defined in the phase image, which significantly simplifies quantitative data analysis. The scatter contrast is dominated by the edges of the samples. This is understandable since the scattering distribution within a pixel is broad at the edges of the sample, which leads to a significant scatter contrast in the projections and consequently in the reconstruction.

3.2.2.4 Alternative Scan Procedures

In addition to the phase-stepping method, several scan and data analysis procedures have been suggested. These approaches aim at reducing the necessary number of acquisitions for phase retrieval. They avoid the need for scanning one grating, which potentially simplifies the experimental setup and image acquisition.

The reverse-projection method (RPM) takes advantage of the fact that the refraction direction of a certain sample feature

is inverted if the sample is rotated by 180° (Zhu et al., 2010). Utilizing this fact in combination with a linear approximation of the PSC yielded the basis for a postdetection algorithm that allows for the retrieval of the absorption and the phase signal (but not the scatter image) from only two projection images.

The Moiré fringe method (MFM) is based on the occurrence of a Moiré pattern in the experimental raw images, when the lines of the two gratings are not parallel to each other. Information about all three contrasts is encoded in the Moiré pattern, which can be retrieved by two-dimensional Fourier analysis of a single image (Momose et al., 2009b). But at the same time, the MFM unavoidably leads to a loss of spatial resolution in the direction perpendicular to the Moiré fringes.

However, the reduced number of acquisitions required for phase retrieval does not necessarily imply a reduction of delivered dose. In fact, the defining quantity for dose efficiency (i.e., sensitivity per delivered dose) is not the number of acquired images, but the number of absorbed photons. It stands to reason that the dose efficiency for the alternative scan procedures is comparable to the phase-stepping technique.

3.3 Experimental Implementation

In this section, details about the experimental implementation of GI are introduced. After presenting the influence of finite coherence, the experimental conditions at a synchrotron beamline (i.e., parallel-beam geometry) as well as with a laboratory source (i.e., cone-beam geometry) are discussed. Further, the manufacturing of high-quality gratings, which are essential for the performance of GI, will be briefly introduced.

3.3.1 Influence of Finite Coherence

A successful experimental implementation of GI requires accounting for the effects of finite coherence and a divergent beam. The implications are briefly discussed in the following.

3.3.1.1 Requirements for Temporal Coherence

A major advantage of the grating interferometer is the low requirements on temporal coherence, which opens up the possibility of phase-sensitive x-ray imaging with x-ray tubes with reasonable acquisition times (Engelhardt et al., 2007; Pfeiffer et al., 2006). It has been shown that the spectral width of the incident beam ζ can be as large as (Weitkamp et al., 2005)

$$\zeta = \frac{1}{2m - 1}, \quad (3.21)$$

which is 1 for the first Lohmann order and still as large as 6×10^{-2} for the 5th Lohmann order.

3.3.1.2 Requirements for Spatial Coherence

The requirement for the spatial coherence is more demanding. Spatial coherence relates to the lateral blurring of interference patterns, which is due to an extended source size (Born and

Wolf, 1999). Simple geometrical considerations show that lateral blurring can be quantified by the projected source size s at the position of the detector (Weitkamp et al., 2006). The projected source size is given by

$$s = dS/l_s \quad (3.22)$$

with d , the beam splitter to detector distance, S , the source size, and l_s , the source to beam splitter distance. In the case of GI, the projected source size s must not be larger than the period of the interference pattern p_2 because otherwise the interference pattern would be smeared out and no contrast would be observable. For synchrotron radiation-based setups with typical lengths of several 10 m, this restriction does not play a crucial role. However, the situation is different for laboratory-based setups.

3.3.1.3 Corrections for Divergent Beams

Up to now, all equations assumed parallel-beam geometry. However, for a cone-beam geometry, the effect of a curved wavefront must be accounted for by adjusting the pitches of the gratings and the intergrating distance. It has been shown (Engelhardt et al., 2008) that the Talbot distance rescales to

$$d_m^* = \frac{l_s d_m}{l_s - d_m} \quad (3.23)$$

and the pitch of the gratings are related by

$$p_2^* = \frac{l_s}{l_s - d_m} \frac{p_1}{2}. \quad (3.24)$$

3.3.2 Instruments Utilizing Synchrotron Radiation

Synchrotron radiation-based setups utilize highly brilliant x-ray sources that offer the advantage of a small beam divergence and high photon flux, which leads to small scan times. In recent years, GI was implemented at several beamlines around the world: at ID19 of the European Synchrotron Radiation facility in France (Weitkamp et al., 2010), at 20XU of Spring-8 in Japan (Momose et al., 2006), at the beamlines 32-ID and 2-BM of the Advanced Photon Source in the United States (Lynch et al., 2011), and at TOMCAT of the Swiss Light Source in Switzerland (McDonald et al., 2009). As an example, the latter will be described in more detail.

Figure 3.5 shows the experimental implementation of GI at the TOMCAT beamline. The x-ray source (not shown) is a 2.9 T bending magnet 25 m upstream from the phase grating. The photon energy (e.g., 25 keV) is selected by a double multilayer monochromator. Both the phase grating (pitch: $p_1 = 3.981 \mu\text{m}$) and the absorption grating (pitch: $p_2 = 2 \mu\text{m}$) were manufactured by the Laboratory for Micro- and Nanotechnology (David et al., 2002). Typically, a Lohmann diffraction order of $m = 2$ is chosen,

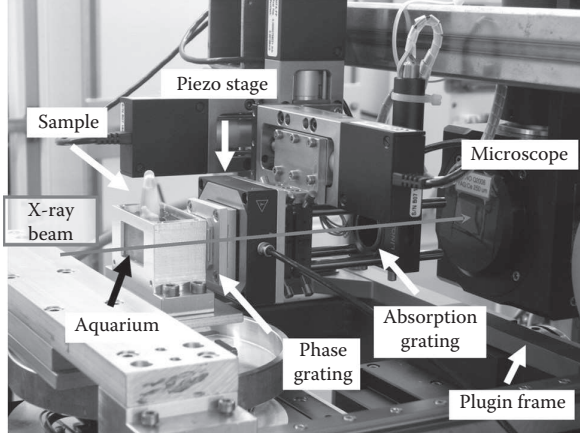


FIGURE 3.5 Grating interferometry at the TOMCAT beamline (Swiss Light Source).

which corresponds to an intergrating distance of $d_2 = 119$ mm. The sample is embedded in 2% agarose gel for mechanical fixation and located in an Eppendorf cylinder. The sample holder is submerged in water for refractive index matching in order to avoid phase wrapping at the edges of the sample. After transmission through the sample and the gratings, the x-ray beam is converted to visible light by a scintillator and subsequently imaged to a charged-coupled device (CCD). A pco.2000 (PCO AG, Kelheim, Germany) CCD camera is used for the detection of the optical photons. It offers an effective dynamic range of approximately 12 bits and a pixel size of $7.4 \mu\text{m}$. The field of view is 12×3.7 mm, which results in a total scanned volume of $12 \times 12 \times 3.7$ mm with an isotropic voxel size of $7.4 \mu\text{m}$. The images shown in Figures 3.4, 3.10, and 3.11 were acquired with the described setup.

3.3.3 Instruments Based on X-Ray Tubes

In comparison to synchrotron radiation-based setups, instruments utilizing an x-ray tube as the source provide the advantage

of low cost and ready accessibility. Thus, for widespread use of any kind of x-ray imaging technique, its feasibility using x-ray tubes is crucial. In this section, two variants of laboratory-based GI setups will be presented.

3.3.3.1 Microfocus X-Ray Tube Setup

As discussed above, the projected source size s at the position of the analyzer grating (Equation 3.22) must be significantly smaller than the period of the interference pattern p_2 . For instance, a total setup length $L = l_s + d$ of 2 m, an intergrating distance of $d = 0.1$ m and a period of $p_2 = 2 \mu\text{m}$ restrict the source size to values smaller than $45 \mu\text{m}$. Thus, microfocus x-ray tubes with typical source sizes in the order of a few microns are the best choice for setups that do not use additional optical elements.

The cone-beam configuration of a microfocus setup (Figure 3.6) opens up the possibility to utilize the geometrical magnification. The closer the sample is placed to the source, the larger it will appear on the detector, with the magnification factor M given by $M = L/l_s$. Since magnification factors of ten and more are feasible, it is possible to achieve micrometer resolution with x-ray detectors providing pixel sizes on the order of several $10 \mu\text{m}$. However, increasing the magnification inevitably decreases the sensitivity to refraction angles. This effect is due to the fact that the lateral shift of the interference pattern decreases with a decreasing source-to-sample distance (Engelhardt et al., 2007). Thus, in experiments, a compromise between the spatial resolution and sensitivity must be found. Figure 3.7 shows example radiographs of a wasp that were obtained with a microfocus setup (Thüring et al., 2011b).

A significant issue of GI with a microfocus tube is the limited field of view (FoV) in the direction perpendicular to the grating lines (i.e., the direction of phase sensitivity). Due to the inclined illumination direction at the borders of the flat analyzer grating, the curved wavefront leads to changes in its transmission function. Consequently, the visibility drops significantly at the border, thus limiting the useable FoV. Therefore, experimental setups were proposed that utilize bent gratings in order to account for the wavefront curvature.

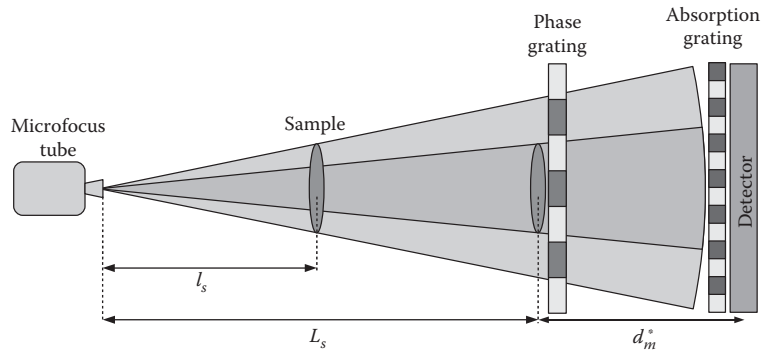


FIGURE 3.6 Grating interferometry with a microfocus x-ray tube.

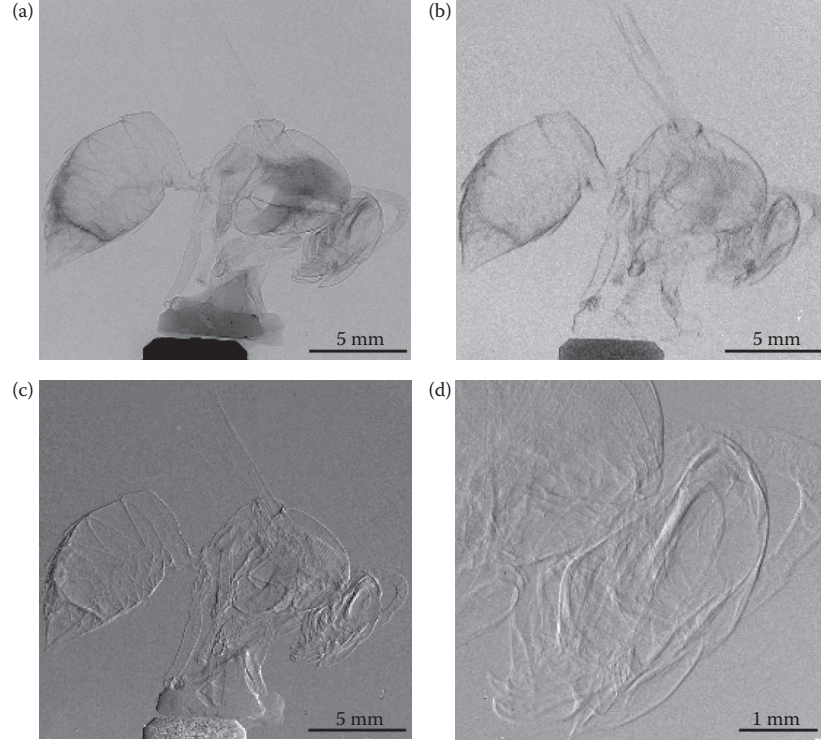


FIGURE 3.7 X-ray radiographs of a wasp acquired with a compact microfocus setup: (a) absorption contrast, (b) scatter contrast, (c) DPC, and (d) DPC with fourfold magnification. (Image courtesy of T. Thüring; from Thüring, T. et al. 2011b. *Proc. SPIE: Phys. Med. Imaging* 7691:79611G.)

A doubling of the usable FoV in the direction of phase sensitivity was already demonstrated (Revol et al., 2010; Thüring et al., 2011a).

3.3.3.2 Talbot–Lau Interferometer

The Talbot–Lau interferometer constitutes an experimental implementation of GI in a laboratory-based setup that allows for larger sources (Chen et al., 2010a; Momose et al., 2009a; Pfeiffer et al., 2006). By including an additional absorption grating close to the source, the limitation of source size, which is implied by Equation 3.22, can be circumvented (Figure 3.8). The source grating creates an array of individually coherent line sources. The line sources are mutually incoherent but if the pitch of the source grating p_0 fulfills the condition

$$p_0 = p_2 \frac{l}{d_m}, \quad (3.25)$$

neighboring line sources provide interference patterns that are shifted by exactly one period. Therefore, all line sources produce the same interference pattern, thus preserving spatial coherence. Simultaneously, the photon flux is increased by a factor that is equal to the number of illuminated periods of the source grating. For instance, a horizontal source size of 0.8 mm and source

grating pitch of 127 μm (Pfeiffer et al., 2006) lead to an increase of photon flux by a factor of 6.

3.3.4 Grating Manufacturing

The availability of high-quality gratings is crucial for the performance of a GI setup in terms of sensitivity, resolution, and artifact-free imaging. A major challenge in manufacturing the gratings is the required high aspect ratio of micrometer line structures. For example, a phase grating that is made of Si and is designed for a photon energy of 40 keV implies a structure height $h = 57 \mu\text{m}$ in order to realize a phase shift of π . Thus, a typical pitch of $p_1 = 4 \mu\text{m}$ leads to an aspect ratio of $A_r = 2h/p_1 \approx 28$. Since the pitch of the analyzer grating is even smaller, aspect ratios of 50 and higher are required for an excellent performance.

In recent years, the production process of the gratings was optimized with respect to the specific combinations of utilized materials (Au for the source and absorption gratings, Si for the phase gratings) and desired aspect ratios. Using a multistep procedure, which consists of photo lithography, anisotropic wet edging, and electroplating (David et al., 2007), high-quality line gratings are now available to fulfill the requirements of GI. Figure 3.9 shows the scanning electron micrographs for two different types of line gratings.

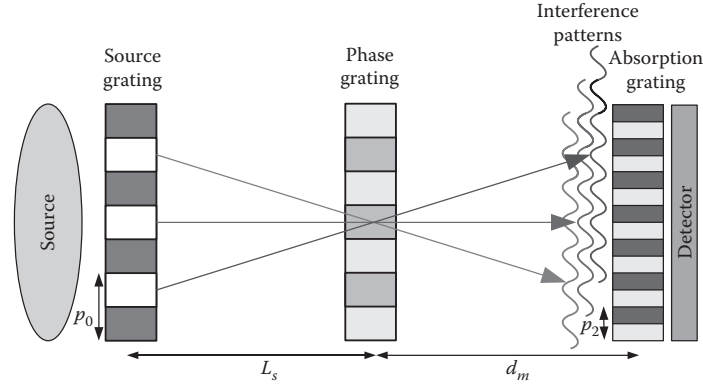


FIGURE 3.8 The Talbot-Lau interferometer.

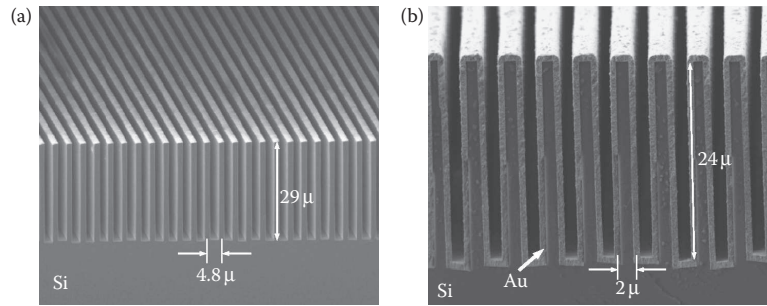


FIGURE 3.9 Scanning electron micrographs of different line gratings: (a) phase grating and (b) analyzer gratings. (Image courtesy of C. David and S. Rutishauser.)

3.4 Biomedical Research and Potential Clinical Application

Due to the unprecedented sensitivity to electron-density variations, GI has already demonstrated its potential for biomedical research. For hard x-rays (i.e., photon energy between 10 and 120 keV) and soft tissues, δ is typically three orders of magnitude larger than β , which directly translates to a corresponding increase in contrast and tissue detectability. Simultaneously, GI offers access to three complementary contrasts (see Section 3.2.2), which opens up the possibility to identify otherwise undetectable sample features. Obviously, this significantly increases the applicability of GI to a wider range of scientific questions. In order to demonstrate these beneficial characteristics of GI, three examples of utilizing GI in the context of biomedical research and potential clinical applications are presented in this section.

3.4.1 Imaging Aortic Heart Valve Calcifications

While the aortic heart valve normally has three leaflets, about 1–2% of the human population have a genetic defect that results in the formation of only two leaflets (termed bicuspid aortic valve (Tzemos et al., 2008)). This is a serious condition that may

severely affect quality of life; heart surgery is often necessary in order to replace the defective heart valve with an artificial valve. Bicuspid aortic valves commonly show calcifications, which constitute the root cause of performance reduction.

Up to now, immunohistochemistry has been the imaging technique of choice for *ex vivo* microscale tissue analysis of extracted heart valves. Although immunohistochemistry offers the capability to readily distinguish between different tissues types, it constitutes a destructive method and provides only limited access to three-dimensional information. In order to overcome these limitations, GI was recently utilized for imaging nodules derived from bicuspid aortic heart valves (Modregger et al., 2012b).

The major challenge of this work was to demonstrate that GI provides a sufficient distinction between tissue types of interest. This was done by taking advantage of the complementary contrasts. More specifically, the availability of the absorption contrast ($\beta \propto Z^n \rho_e$, Equation 3.13) and the phase contrast ($\delta \propto \rho_e$, Equation 3.17) opens up the possibility to retrieve the effective atomic number map \tilde{Z} with

$$\tilde{Z} = \frac{\beta}{\delta} = f(Z),$$

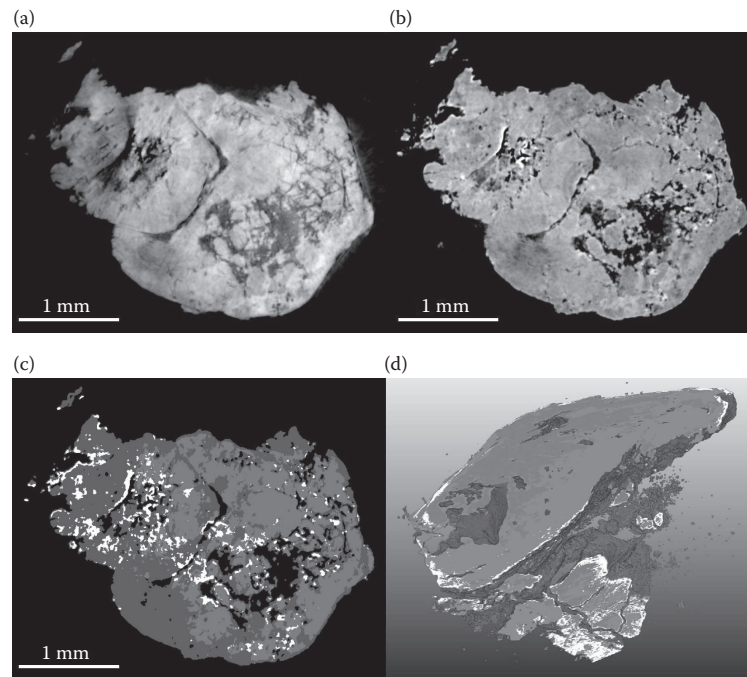


FIGURE 3.10 (See color insert.) Microstructural analysis of a calcified nodule derived from a bicuspid aortic heart valve: (a) electron density map, (b) effective atomic number map, (c) segmented tissue of the same slice, and (d) 3D visualization of the entire segmented sample. Blue: myxoid tissue, red: dense tissue, and white: regions of elevated calcium concentration.

which is only a function of the material property Z (i.e., the atomic number). By combining the information of the accessible contrasts (i.e., β , δ , and \tilde{Z}), it was possible to segment otherwise indistinguishable tissue types.

Figure 3.10 shows the approach and the result of the segmentation process. It is obvious that the electron density map (a) and the effective atomic number map (b) provide complementary information about the inner morphology of a calcified nodule. On the one hand, dense and myxoid (i.e., loose) connective tissue appear as bright and dark areas in (a), while being almost indistinguishable in (b). On the other hand, regions of elevated calcium concentration appear as bright spots in (b), while being absent in (a). Figure 3.10c and d presents the result of combining these complementary contrasts into a single segmentation. This example demonstrates that GI provides the possibility of destruction-free, three-dimensional microstructural analysis with sufficient sensitivity to distinguish among tissue types. Therefore, GI could play a significant role in future medical research of cardiovascular diseases with the potential to be used complementary or even as an alternative to histology.

3.4.2 Imaging Alzheimer's Plaque Deposits in a Mouse Model

The unique pathological characteristic of Alzheimer's disease is the accumulation of a specific peptide from the amyloid precursor protein into spherical agglomerates—so-called amyloid

plaques—in the extracellular space of the brain (Reitz et al., 2011). These plaques are believed to play an important role in the biochemical chain that finally leads to cognitive impairment and dementia. The problem with plaque detection and visualization is their small size: in humans, amyloid plaques are typically on the order of 25 μm . Imaging techniques like positron emission tomography provide an overview of the plaque load in a living patient, but imaging single plaques remains a big challenge.

Mouse models with the same pathology have been developed to study various aspects of plaques, including possible treatments to dissolve them. But in order to reveal the precise amount and locations of plaques, the brain needs to be sliced and treated with dyes. In certain mouse models with larger plaques ($\sim 75 \mu\text{m}$ and larger), magnetic resonance imaging has been shown to be able to detect some plaques, but this is at the limit of resolution.

With the sensitivity and resolution provided by GI, the plaque population of a mouse brain can be measured and automatically segmented *ex vivo*, revealing complete structural information. Figure 3.11a shows a close up of the phase-data reconstruction, which was acquired by GI with eight phase steps at 25 keV. The coronal cross section of the entire brain fit into the field of view, which permitted acquisition of a complete overview of the plaque distribution. The plaque pathology is clearly visible (i.e., small, dark spots). Image processing for normalization of the images and automated segmentation revealed the set of amyloid plaques, which is shown within a region of interest—the cerebral cortex—in panel (b). The measurements as well

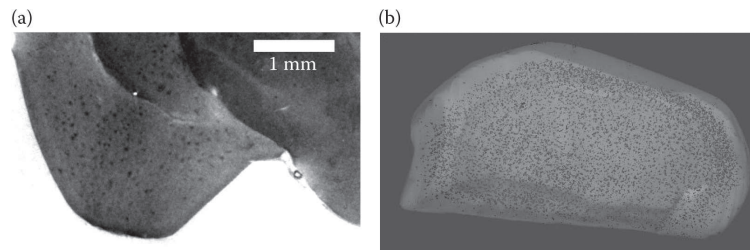


FIGURE 3.11 (See color insert.) Amyloid plaque deposit in the cerebral cortex of a mouse model as revealed by GI: (a) zoom into a phase reconstruction slice and (b) a 3D rendering of the segmented mouse brain with the cerebral cortex in gray and amyloid plaques in red.

as the image-processing steps are described in detail in Piner et al. (2012). This example again elucidates the advantages of GI for biomedical imaging: the sensitivity to distinguish different types of soft tissue, coupled with high resolution and a large field of view.

3.4.3 Potential for Mammography

So far, in clinical applications like radiography, mammography, or computed tomography, only x-ray attenuation has been used for image generation. As demonstrated in this chapter, GI offers a significantly higher sensitivity to density variations in soft tissues at clinically relevant photon energies. Thus, GI can potentially revolutionize the radiological approach to medical imaging. Further, the availability of the scatter contrast can be used to increase the diagnostic utility of minute sample features (see Figure 3.3). In the following, the exciting potential of GI for future mammography is suggested with an example.

Breast cancer is the most common cancer in women and the second leading cause of cancer deaths (Kamangar et al., 2006). International standards for diagnostics and treatment are not stringently followed and it is estimated that 35% of all breast

cancer deaths in Europe could be avoided if optimal diagnostic and therapeutic procedures were always applied. In the United States, the age-adjusted incidence rates of breast cancer rose rapidly between 1980 and 1987, and they are also rising rapidly in several Asian countries (e.g., Japan), which currently have the lowest incidence rates. This may indicate that, besides genetic predisposition, environmental factors, for example, estrogen-replacement therapy, oral contraceptives, dietary factors, or alcohol consumption may play an additional role (Kelsey, 1993). Improving the sensitivity and specificity of the mammographic examination without increasing the dose applied to the patient is therefore of crucial importance. Recently, an exploratory study showed the world's first phase-contrast mammography images of native (not fixed) human breast using a conventional x-ray source (Stampanoni et al., 2011).

Figure 3.12 clearly shows how the high-frequency components in a mammographic image can be enhanced when the differential phase-contrast signal is merged into the conventional absorption signal, to yield a much sharper image. The novel approach yields complementary and otherwise inaccessible information on the electron density distribution and the small-angle scattering power of the sample at the microscopic

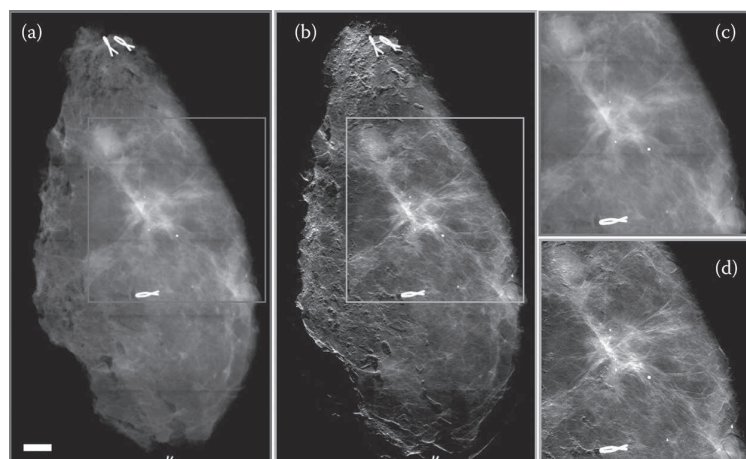


FIGURE 3.12 Freshly dissected tissue (mastectomy specimens) imaged with conventional (a) and phase-contrast-enhanced mammography (b). Panels (c) and (d) show the corresponding magnified regions marked in (a) and (b), respectively. Images (a) and (b) have been obtained with the same dose. Scale bar in (a) is 2 cm. Data has been acquired with a conventional x-ray source with a Talbot–Lau interferometer operated at 28 keV.

scale. Potentially, this could answer clinically relevant, yet unresolved, questions such as the capability to unequivocally discern between malignant, premalignant changes, and post-operative scars or to identify cancer-invaded regions within healthy tissue.

Acknowledgments

The authors like to acknowledge Thomas Thüning, Simon Rutishauser, and Christian David of the Paul Scherrer Institut (Villigen, Switzerland) for their contributions in the form of raw data and images.

References

- Banaszek, K., K. Wodkiewicz, and W. Schleich. 1997. Fractional Talbot effect in phase space: A compact summation formula. *America* 117:4.
- Bech, M., O. Bunk, T. Donath et al. 2010. Quantitative x-ray dark-field computed tomography. *Phys. Med. Biol.* 55:5529.
- Bech, M., T.H. Jensen, R. Feidenhans'l et al. 2009. Soft-tissue phase-contrast tomography with an x-ray tube source. *Phys. Med. Biol.* 54:2747.
- Born, M., and E. Wolf. 1999. *Principles of Optics*. Cambridge University Press, Oxford, England.
- Chen, G.-H., N. Bevins, J. Zambelli, and Z. Qi. 2010a. Small-angle scattering computed tomography (SAS-CT) using a Talbot-Lau interferometer and a rotating anode x-ray tube: Theory and experiments. *Opt. Express* 18:12960.
- Chen, R.C., R. Longo, L. Rigon et al. 2010b. Measurement of the linear attenuation coefficients of breast tissues by synchrotron radiation computed tomography. *Phys. Med. Biol.* 55:4993.
- David, C., J. Bruder, T. Rohbeck et al. 2007. Fabrication of diffraction gratings for hard x-ray phase contrast imaging. *Microelectron. Eng.* 84(5–8):1172.
- David, C., B. Nöhammer, H.H. Solak, and E. Ziegler. 2002. Differential x-ray phase contrast imaging using a shearing interferometer. *Appl. Phys. Lett.* 81:3287.
- Engelhardt, M., J. Baumann, M. Schuster et al. 2007. High-resolution differential phase contrast imaging using a magnifying projection geometry with a microfocus x-ray source. *Appl. Phys. Lett.* 90:224101.
- Engelhardt, M., C. Kottler, O. Bunk et al. 2008. The fractional Talbot effect in differential x-ray phase-contrast imaging for extended and polychromatic x-ray sources. *J. Microsc.* 232:145.
- Jerjen, I., V. Revol, P. Schuetz et al. 2011. Reduction of phase artifacts in differential phase contrast computed tomography. *Opt. Express* 19(14):13604.
- Kak, A.C., and M. Slaney. 1988. *Principles of Computerized Tomographic Imaging*. IEEE Press, New York, USA.
- Kamangar, F., G.M. Dores, and W.F. Anderson. 2006. Patterns of cancer incidence, mortality, and prevalence across five continents: Defining priorities to reduce cancer disparities in different geographic regions of the world. *J. Clin. Oncol.* 24(14):2137.
- Kelsey, J.L. 1993. Breast-cancer epidemiology—Summary and future-directions. *Epidemiol. Rev.* 15(1):256.
- Khelashvili, G., J.G. Brankov, D. Chapman et al. 2006. A physical model of multiple-image radiography. *Phys. Med. Biol.* 51:221.
- Lynch, S.K., V. Pai, J. Auxier et al. 2011. Interpretation of dark-field contrast and particle-size selectivity in grating interferometers. *Appl. Optics* 50:4310.
- McDonald, S.A., F. Marone, C. Hintermüller et al. 2009. Advanced phase-contrast imaging using a grating interferometer. *J. Synchrotron Radiat.* 16(Pt 4):562.
- Modregger, P., B.R. Pinzer, T. Thüning et al. 2011a. Sensitivity of x-ray grating interferometry. *Opt. Express* 19:18324.
- Modregger, P., F. Scattarella, B.R. Pinzer et al. 2012a. Imaging the ultrasmall-angle x-ray scattering distribution with grating interferometry. *Phys. Rev. Lett.* 108(4):048101.
- Modregger, P., Z. Wang, T. Thüning, B. Pinzer, and M. Stampanoni. 2011b. Artifacts in x-ray dark-field tomography. *AIP Conf. Proc.* 1365:269.
- Modregger, P., B. Weber, B.R. Pinzer et al. 2012b. Micro-structural analysis of human bicuspid aortic valve derived nodules using x-ray grating interferometry. *Phys. Med. Biol.* submitted.
- Momose, A. 2004. Phase tomography using an x-ray Talbot interferometer. *Proc. SPIE.* 5535:352.
- Momose, A., S. Kawamoto, I. Koyama et al. 2003. Demonstration of x-ray Talbot interferometry. *Jpn. J. Appl. Phys.* 42:L866.
- Momose, A., W. Yashiro, H. Kuwabara, and K. Kawabata. 2009a. Grating-based x-ray phase imaging using multiline x-ray source. *Jpn. J. Appl. Phys.* 48:076512.
- Momose, A., W. Yashiro, H. Maikusa, and Y. Takeda. 2009b. High-speed x-ray phase imaging and x-ray phase tomography with Talbot interferometer and white synchrotron radiation. *Opt. Express* 17:12540.
- Momose, A., W. Yashiro, Y. Takeda, Y. Suzuki, and T. Hattori. 2006. Phase tomography by x-ray Talbot interferometry for biological imaging. *Jpn. J. Appl. Phys.* 45:5254.
- Müller, B., S. Lang, M. Dominietto et al. 2008. High-resolution tomographic imaging of microvessels. *Proc. SPIE.* 7078: 70780B.
- Pfeiffer, F., M. Bech, O. Bunk, P. Kraft, and E.F. Eikenberry. 2008. Hard-x-ray dark-field imaging using a grating interferometer. *Nat. Mat.* 7(2):134.
- Pfeiffer, F., O. Bunk, C. David et al. 2007a. High-resolution brain tumor visualization using three-dimensional x-ray phase contrast tomography. *Phys. Med. Biol.* 52:6923.
- Pfeiffer, F., O. Bunk, C. Kottler, and C. David. 2007b. Tomographic reconstruction of three-dimensional objects from hard x-ray differential phase contrast projection images. *Nucl. Instrum. Meth. A* 580:925.
- Pfeiffer, F., C. Kottler, O. Bunk, and C. David. 2007c. Hard x-ray phase tomography with low-brilliance sources. *Phys. Rev. Lett.* 98:1.
- Pfeiffer, F., T. Weitkamp, O. Bunk, and C. David. 2006. Phase retrieval and differential phase-contrast imaging with low-brilliance x-ray sources. *Nature Phys.* 2:258.

- Pinzer, B.R., M. Cacquevel, P. Modregger, S.A. McDonald, J.C. Bensadoun, T. Thuering, P. Aebischer, M. Stampanoni. July 2012. Imaging brain amyloid deposition using grating-based differential phase contrast tomography. *NeuroImage* 61(4):1336–1346.
- Qi, Z., J. Zambelli, N. Bevins, and G.-H. Chen. 2010. Quantitative imaging of electron density and effective atomic number using phase contrast CT. *Phys. Med. Biol.* 55:2669.
- Rayleigh, L. 1881. Experiments with and theory of diffraction gratings. *Phil. Mag.* 11:196.
- Reitz, C., C. Brayne, and R. Mayeux. 2011. Epidemiology of Alzheimer disease. *Nat. Rev. Neurol.* 7(3):137.
- Revol, V., C. Kottler, R. Kaufmann et al. 2010. X-ray interferometer with bent gratings: Towards larger fields of view. *Nucl. Instrum. Meth. A* 648:302.
- Schulz, G., T. Weitkamp, I. Zanette et al. 2010. High-resolution tomographic imaging of a human cerebellum: Comparison of absorption and grating-based phase contrast. *J. R. Soc. Interface* 7:1665.
- Stampanoni, M., Z. Wang, T. Thüring et al. 2011. The first analysis and clinical evaluation of native breast tissue using differential phase-contrast mammography. *Invest. Radiol.* 46(12):801.
- Suleski, T.J. 1997. Generation of Lohmann images from binary-phase Talbot array illuminators. *Appl. Optics* 36:4686.
- Talbot, H.F. 1836. LXXVI. Facts relating to optical science. No. IV. *Phil. Mag. Series 3* 9:401.
- Thüring, T., P. Modregger, T. Grund et al. 2011a. High resolution, large field of view x-ray differential phase contrast imaging on a compact setup. *Appl. Phys. Lett.* 99:041111.
- Thüring, T., P. Modregger, B.R. Pinzer et al. 2011b. Towards x-ray differential phase contrast imaging on a compact setup. *Proc. SPIE: Phys. Med. Imaging* 7691: 79611G.
- Tzemos, N., J. Therrien, J. Yip et al. 2008. Outcomes in adults with Bicuspid Aortic Valves. *Jama-J. J. Am. Med. Assoc.* 300(11): 1317.
- Wang, Z.-T., K.-J. Kang, Z.-F. Huang, and Z.-Q. Chen. 2009. Quantitative grating-based x-ray dark-field computed tomography. *Appl. Phys. Lett.* 95:094105.
- Weitkamp, T., C. David, C. Kottler, O. Bunk, and F. Pfeiffer. 2006. Tomography with grating interferometers at low-brilliance sources. *Proc. SPIE.* 63180S.
- Weitkamp, T., A. Diaz, C. David et al. 2005. X-ray phase imaging with a grating interferometer. *Opt. Express* 13:6296.
- Weitkamp, T., I. Zanette, C. David et al. 2010. Recent developments in x-ray Talbot interferometry at ESRF-ID19. *Proc. SPIE.* 7804:780406.
- Yashiro, W., Y. Terui, K. Kawabata, and A. Momose. 2010. On the origin of visibility contrast in x-ray Talbot interferometry. *Opt. Express* 18(16):16890.
- Zhu, P., K. Zhang, Z. Wang et al. 2010. Low-dose, simple, and fast grating-based x-ray phase-contrast imaging. *P. Natl. Acad. Sci. U.S.A.*